Effect of magnetic-spring bi-stable nonlinear energy sink on vibration and damage reduction of concrete double-column piers: experimental and numerical analysis

Jundong Fu[a,b], Shui Wan[a*], Peng Zhou[a], Jiwei Shen[a], Mia Loccufier[b] and Kevin Dekemele[b]

[a]School of Transportation, Southeast Univ., Nanjing, 211189 Jiangsu, China.

[b]Department of Electromechanical, Systems and Metal Engineering, Ghent Univ., Ghent, 9052, Belgium.

E-mail addresses:

Jundong.Fu@UGent.be (Jundong Fu);

lanyu421@163.com (ShuiWan);

zhoupeng_1122@163.com (Peng Zhou);

shenjiwei200888@163.com (Jiwei Shen);

Mia.Loccufier@UGent.be (Mia Loccufier);

Kevin.Dekemele@UGent.be (Kevin Dekemele).

*Correspond author: Email address: lanyu421@163.com (S.Wan)

Abstract: Concrete structures suffer from crack damage under heavy vibrations, caused by seismic loads. Passive vibration control devices can be used to reduce the damage. The most common device is the tuned-mass-damper (TMD), which is tuned to match the natural frequency of the primary structure. However, under prolonged vibration load, the natural frequency of the concrete structure decreases, reducing the TMD's effectiveness in mitigating vibrations and damage, as it can only target a fixed natural frequency. Therefore, this study will propose and implement the nonlinear energy sink (NES), which is a vibration control device that can adapt to changing frequency, resulting in a larger effective bandwidth than the TMD. As a concrete structure, the cast-in-place double-column piers is seismically loaded with a shaking table with and without NES to observe the vibration and damage-mitigating properties of the NES. More specifically, a magnetic bi-stable NES (MBNES) with a viscous fluid damper (VFD) is designed and built. The bi-stable restoring force allows for a larger bandwidth than conventional NESs, and the magnets and VFD allow for easy manufacturability. An optimization method is proposed to obtain optimal parameters, and the restoring force and damping of the experimentally designed MBNES are verified using the restoring force surface method. The proposed design, optimization and identification procedure are generic and can be applied to any (concrete) civil structure. Shaking table tests are used to verify the robust performance of MBNES under continuous changes in the natural frequency of concrete double-column piers. The experimental results show that the MBNES can effectively mitigate vibrations of the pier and, consequently, reduce the damage of the pier, slow down the decrease of the stiffness of the

pier, reduce the curvature and shear deformation of the pier. Numerical analysis results show that MBNES can absorb the energy of the primary structure in a wide frequency bandwidth and has excellent robust performance compared to conventional devices.

Key words: Bridge engineering; Magnet-spring bi-stable energy sink; Dynamic control; Shake table experiment; Numerical analysis; Bouc-wen model; Robust performance.

1. Introduction

In the field of civil engineering, vibration control is of paramount importance in structures such as buildings and bridges. Currently, the most common vibration control device is the tuned mass damper (TMD), which is able to efficiently damp excessive vibrations near the natural frequency of the primary structure. However, if the dynamic characteristics of the primary structure change, or if the vibration energy is not concentrated in the natural frequency vibration, its damping effect will be seriously compromised. Pinkaew et al. discovered that while TMD can diminish the damage to the initial concrete structure during an earthquake, it cannot further mitigate the structure's response after sustaining damage [1]. Rahimi et al. considered that the TMD focus solely on tuning to the dominant frequency rather than accounting for all natural frequency of the structure. In continuous seismic wave loading, as the natural frequency of the primary structure changes, the efficacy of the TMD in controlling vibrations diminishes [2]. Recently, a device called nonlinear energy sink (NES) featuring broadband damping characteristics has attracted more and more scholars' attention. The broader frequency band is a consequence of the nonlinear restoring force in the NES, typically a hardening nonlinearity, which allows the NES to self-tune its natural frequency to the frequency of primary structure. Many scholars have done relevant research in order to apply the NES in the field of civil engineering [3-4]. Gourdon et al. [5-8] designed a cubic NES to conduct theoretical, numerical and experimental studies on vibration reduction of a single-story metal frame and a four-story frame structures, respectively. The results showed that the oscillators with a strong nonlinearity could effectively absorb the vibrations of the primary structure without reflecting energy back to the primary structure. Nucera et al. [9] conducted an experimental study on a vibro-impact (VI) NES attached on the top of a three-layer frame and found that VI NES had excellent and robust performance. Quinn et al. [10] coupled an NES with strong nonlinearity to a two-degree-of-freedom (DOF) frame structure. Through experiment and numerical analysis, that the NES can effectively reduce the vibration of the frame structure under the shock load. Al-Shudeifat et al. [11-14] carried out numerical and experimental research on the vibration reduction effect of a rotary NES on a multi-DOF building model. In particular, the targeted energy transfer (TET) mechanism, frequency-energy plot and robustness of the rotary NES were deeply studied. Wierschem et al. [15-18] focused on the dynamic performance of multi-DOF frame structures coupled with different NESs under explosive impact loads. The experimental results showed that the NES could rapidly mitigate the vibration of the primary structure. Wang et al. [19-22] studied on the track NES and discovered rapid energy absorption and high robustness in building structures. Compared with other types of NESs, the vibration absorption performance was similar. Dekemele et al. [23-24] introduced the design principle and control equation of a novel NES. He analyzed the dynamic characteristics of the NES coupled to a single DOF frame structure using the harmonic balance method. Experiments verified the damping characteristics and the restoring force surface method identified the nonlinear force equation in the NES. It should be noted that almost all works focus on linear primary structures made via metal.

So far, many scholars have proposed different kinds of NES, such as cubic NES (CNES), bi-stable NES (BNES), track NES and so on [8, 19-39]. Among these NESs, using permanent magnets to provide nonlinear restoring force has become a hot research topic [40-46]. Al-Shudeifat [40] introduced an asymmetric magnetic restoring force into the NES. Compared to the NES with symmetrical stiffness, this design can significantly enhance its damping performance. Chen et al. [41-43] constructed an NES using four pairs of permanent magnets with bi-stable characteristics. The optimal multiple design parameters in the NES were obtained by global optimization. Compared with TMD and CNES, the BNES can produce wide-frequency band and rich internal resonance behavior with the primary structure. Therefore, it can combat the performance degradation of traditional vibration control devices oscillators in the field of civil engineering caused by due to the changes in structural dynamic characteristics, such as those caused by concrete damage. At the same time, the permanent magnets can provide a non-contact smooth nonlinear restoring force, and combined with a linear spring forms a BNES, which own broad application prospects in the field of civil engineering vibration reduction [38, 41-42]. In addition, there are few studies on vibration reduction control using NES for concrete-based structures, and have not studied the damage reducing abilities of the NES [47]. As such, a gap in the literature and the focus of the current paper is the experimental study of the MBNES in reducing damage in concrete structures, and its performance under decreasing natural frequency of concrete primary structures under continuous damage process. As a concrete structure, two concrete double-column piers are cast, one that will feature the MBNES and one without a vibration control device. The damage is induced by a shaking table with seismic waves of increasing energy levels. The optimization and identification method used here allows for easy manufacturability for civil engineering applications, as the proposed and built NES consists of magnets, linear springs, and viscous fluid dampers that are readily available from manufacturers. This paper is structured as follows: In section 2, the dimensions, material properties and sensors arrangement of the double-column piers are introduced in detail. In addition, the description and parameters optimization of MBNES and parameters identification using restoring force method of MBNES are also described. In the 3rd section, the experimental effectiveness of the MBNES for vibration control and damage reduction of the double-column piers are verified via experimental method with shaking table test of increasing magnitude. In the section 4, the numerical simulation results using the Bouc-Wen model are compared with the experimental results, while the vibration control performance of the MBNES is compared to that of the TMD, under decreasing natural frequency of the primary concrete structure. Finally, the conclusions are stated.

2. Experimental design and setup

2.1 Primary structure and sensors arrangement

The geometric dimensions and the sensor arrangement of the cast-in-place (CIP) double-column piers are presented in Table 1 and Fig. 1. The sensors will be used to assess vibration levels and damage. The reinforcement ratio and volumetric stirrup ratio of the piers are 1.1% and 0.84%, respectively. The piers without and with NES will be referred to in the rest of the text as CIP-1 and CIP-2.

Table 1 The specific design parameters of the CIP double-column piers

Component	Size (mm^3)	Component	Size (mm)
Cap	3300×550×350	Cover thickness	30
Column	240×240×1300	Effective height of piers	1750
Footing	2400×720×360	Reinforcement	ϕ10@90
Concrete plate	3100×2400×550	Stirrup	ϕ6@75

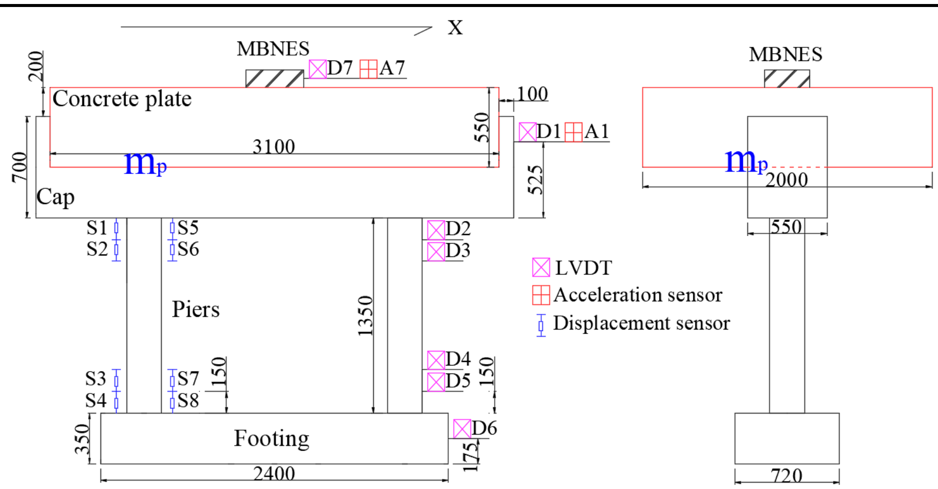

Fig. 1 Design details and sensors arrangement of CIP double-column piers (unit: mm)

The standard compressive strength of concrete is measured according to the *Standard for test method of concrete structures (GB/T50152-2012)* [48]. The 28-day average compressive strength of the six standard concrete cubes (150×150×150 mm^3) is

35.9 MPa and the elastic modulus of concrete is 3.1×10^4 MPa. The density of the concrete is 2.42 t/m^3. Therefore, the mass (containing concrete plate and the cap) of the primary structure m_p is 9.91 t. Table 2 shows the average yield and tensile strength of the reinforcement and stirrup. The test was carried out according to the standards of *Metallic materials-Tensile testing at ambient temperature (GB/T228.1-2010)* [49].

Table 2 Property parameters of reinforcement and stirrup

Type	Grade	Diameter (mm)	Yield strength (MPa)	Tensile strength (MPa)	Elastic modulus (MPa)	Fracture strain (%)
Reinforcement	HRB400	10	431.63	553.33	2×10^5	17.1
Stirrup	HRB400	6	423.22	539.52	2×10^5	17.6

Meanwhile, as depicted in Fig. 1, the displacement sensors (S1 to S8) were arranged at the height of 150 mm and 300 mm below the cap and over the footing of the pier to obtain the curvature distribution. The displacement sensors D1 and D6 measured the displacement of the cap and footing, respectively. The displacement sensors D2 to D5 respectively obtained the horizontal displacement of the pier body under the seismic load. D3 and D2 were arranged at 150 mm and 300 mm from the bottom of the cap. D5 and D4 were arranged at 150 mm and 300 mm from the top of the footing. Additionally, the displacement sensor D7 measures the displacement of the MBNES for CIP-2. Both the shaking table and the oscillator move along the strong axis direction (X) of the double-column piers.

2.2 Proposed MBNES

The schematic and realization of the MBNES are shown in Fig.2. The MBNES consists of 16 magnets, two linear springs, a viscous fluid damper (VFD), a mass block, four roller bearings and two sliding rails. The dimensions of the mass block are shown in Fig. 2(b) and the volume is 0.0204 m^3. The repulsive force between the magnets realizes the nonlinear restoring force. Compared with the other MBNESs [32, 39], the springs are used in the movement direction of the oscillator, which not only provides additional restoring force but also facilitates the installation of the VFD. The springs in the MBNES device are made of 60Si2MnA steel, the cylinder body of VFD is made of tin bronze, and the other parts are made of non-magnetic stainless steel which density is 7930 kg/m^3. The whole device does not contain any ferromagnetic material. The weight of the oscillator (m_l) is 198.2 kg consisting of the weight of the mass block and the weight of the magnets attached to the mass block. Hence, the mass ratio of the MBNES to the primary structure is set as 2%.

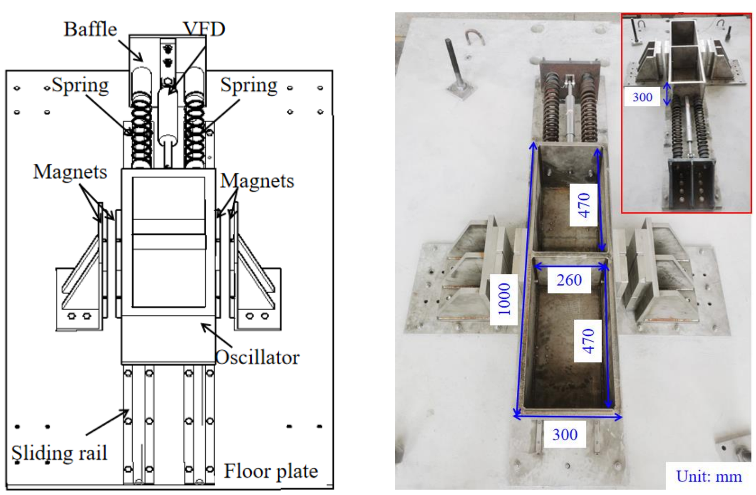

(a) (b)

Fig. 2 Design of MBNES: (a) schematic; and (b) realization.

The proposed MBNES contains one unstable point and two stable points, and the schematic diagram is shown in Fig. 3. Fig. 3 (a) displays the unstable point of MBNES.

Then, the spring is at its original length and the magnets are completely parallel. Fig. 3 (b) and (c) show the two stable points in the MBNES, and the spring is in a compressed or stretched state.

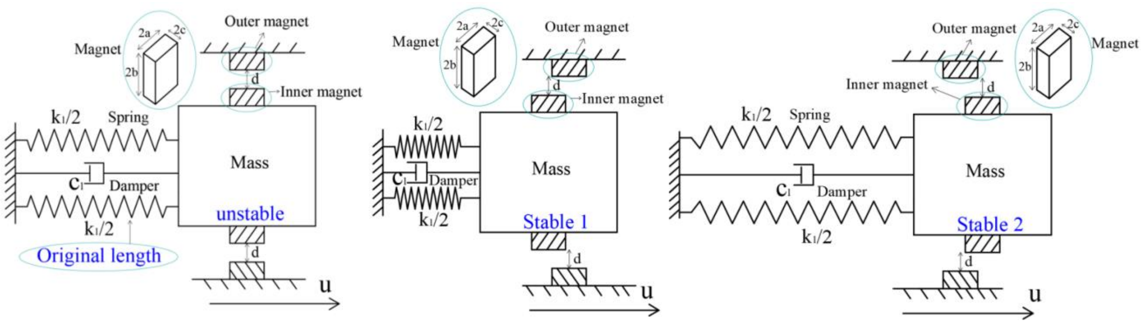

(a) (b) (c)

Fig. 3 Schematic points of MBNES: (a) unstable point; (b) stable point 1; and (c) stable point 2.

2.3 Parameters optimization of MBNES

The linearized equations of motion of the double-column piers coupled with MBNES are:

$$\begin{cases} m_p\ddot{x}_p + c_p\dot{x}_p + k_p x_p - c_l\dot{u} - F = -m_p\ddot{x}_g \\ m_l\ddot{u} + c_l\dot{u} + F = -m_l(\ddot{x}_g + \ddot{x}_p) \end{cases} \tag{1}$$

Where the natural angular frequency ω_n of the double-column piers is 37.13 rad/s, which was obtained from the excitation tests, and the equivalent stiffness k_p of the piers is 13665 kN/m. According to the standard [50], the equivalent viscous damping ratio ξ of concrete structures is 0.05, meaning a damping coefficient of the primary structure c_p of 36.8 kN·s/m. x_p, $\dot{x}_p$ and $\ddot{x}_p$ are the displacement, velocity and acceleration relative to the ground motion of the cap, respectively. $\ddot{u}$ and $\dot{u}$ are the relative acceleration and velocity between the oscillator and the cap, respectively. F is the restoring force provided by the MBNES. $\ddot{x}_g$ is the base acceleration. c_l is the viscous damping coefficient of

VFD.

An optimization is required to create the MBNES design capable of minimizing the primary structure's response to impulsive loads. Additionally, ensuring the system's resilience to changes in the primary structure's natural frequency over time is another objective of this optimization. The optimization will be carried out on Eq.(1), which has a linear elastic concrete model, in order to apply the techniques of [43] and [50]. In [43], in order to evaluate the performance of the MBNES, the peak displacement response, the energy of the controlled (E_p) and uncontrolled primary structures ($E_{p,0}$), the root mean square (RMS) displacement responses of the controlled (D_{RMS}) and uncontrolled primary structure ($D_{RMS,0}$) are compared. The objective function I is defined as the weighted performance measures $E_P/E_{P,0}$ and $D_{RMS}/D_{RMS,0}$, that is Eq.(2).

$$I = \min\left(\frac{1}{2}\frac{E_P}{E_{P,0}} + \frac{1}{2}\frac{D_{RMS}}{D_{RMS,0}}\right), \quad where \quad \frac{E_P}{E_{P,0}} = \frac{c_p \sum_{i=1}^{n} \dot{x}_p^2(i)dt}{c_P \sum_{i=1}^{n} \dot{x}_{P,0}^2(i)dt} \tag{2}$$

Where $\dot{x}_{p,0}$ represents the velocity of the uncontrolled primary structure.

To calculate the restoring force (repulsion force) of the magnets in the movement direction of the oscillator, the equivalent magnetic charge model is considered [39]. In order to remove a net perpendicular force on the mass, the magnets on both sides of the oscillator are equivalent. The restoring force of BMNES can be expressed as Eq. (3) to Eq. (5).

$$F = k_l u + \frac{-J^2}{4\pi\mu_0}\sum_{i=0}^{1}\sum_{j=0}^{1}\sum_{k=0}^{1}\sum_{l=0}^{1}\sum_{p=0}^{1}\sum_{q=0}^{1}(-1)^{i+j+k+l+p+q}[2\Phi(u,d+c)] \quad (3)$$

Where

$$\Phi(u,d+c) = \frac{Y_{kl}^2 - Z_{pq}^2}{2}\ln(S - X_{ij}) + X_{ij}Y_{kl}\ln(S - Y_{kl}) + Y_{kl}Z_{pq}\arctan(\frac{X_{ij}Y_{kl}}{SZ_{pq}}) + \frac{1}{2}SX_{ij} \quad (4)$$

$$\begin{cases} X_{ij} = u + (-1)^j a - (-1)^i a & Y_{kl} = (-1)^j b - (-1)^i b \\ Z_{pq} = (b+c) + (-1)^q c - (-1)^p c & S = \sqrt{X_{ij}^2 + Y_{kl}^2 + Z_{pq}^2} \end{cases} \quad (5)$$

Where J is the polarization intensity of the magnets with a value of 1.34 T, μ_0 is the vacuum permeability factor ($4\pi\times10^{-7}$ H/m) [41]. Parameters 2*a*, 2*b* and 2*c* are the length, height and thickness of the magnets, and *d* is the net distance between two magnets. k_l is the stiffness of two springs.

The first step in the optimization scheme is computing the TMD design parameters k_{opt} and c_{opt} based on the natural frequency of the primary structure [48-50]. These will be used to define a parameter range for the springs (k_l) and viscous damper (c_l) used in the MBNES. These parameters are calculated by Eq.(6) .

$$\begin{cases} f_{opt} = \frac{1}{1+\gamma}(\sqrt{\frac{2-\gamma}{2}}) & \varsigma_{opt} = \sqrt{\frac{3\gamma}{8(1+\gamma)}}(\sqrt{\frac{2}{2-\gamma}}) \\ k_{opt} = f_{opt}^2\Omega^2 m_l & c_{opt} = 2\varsigma_{opt} f_{opt}\Omega \end{cases} \quad (6)$$

Where k_{opt} and c_{opt} are 260 kN/m and 6.21 kN/(m/s). The global optimization method is used to find the minimum value of the Eq. (2). The assessment of MBNES's vibration reduction efficiency involves applying an initial velocity of 0.8 m/s to the primary structure, allowing the oscillator within MBNES to consistently undergo steady-state transitions [19, 39, 49, 51]. Furthermore, using an impulsive load makes the optimization independent of used seismic waves. The fourth-order Runge-Kutta method is used to calculate the Eq. (1). Considering the MBNES devices can be made easily in the factory, the parameters, optimization scope of parameters, optimization step size, optimal value and the value of I_{min} are shown in Table 3. For each step, the objective function I is computed.

Table 3 Optimization parameters of MBNES

Device	Parameter	Optimization scope	Optimization step size	Optimal value	I_{min}
MBNES	2a (mm)	100~300	20	200	0.448
	2b (mm)	200~400	20	300	
	2c (mm)	10~30	5	25	
	d (mm)	10~30	2	10	
	k_l (kN/m)	130~390	26	156	
	c_l (kN/(m/s))	1.5525~7.7625	0.621	1.5525	

Fig. 4 (a) displays the displacement of the primary structures under the control of the optimal MBNES parameters and TMD parameters, respectively. The displacement decay of the primary structure under MBNES control is faster than those under TMD control. The oscillator in MBNES, as depicted in Fig. 4(b), exhibits steady-state transitions and moves at a higher speed compared to TMD. This indicates that MBNES absorbs and consumes energy more rapidly from the primary structure.

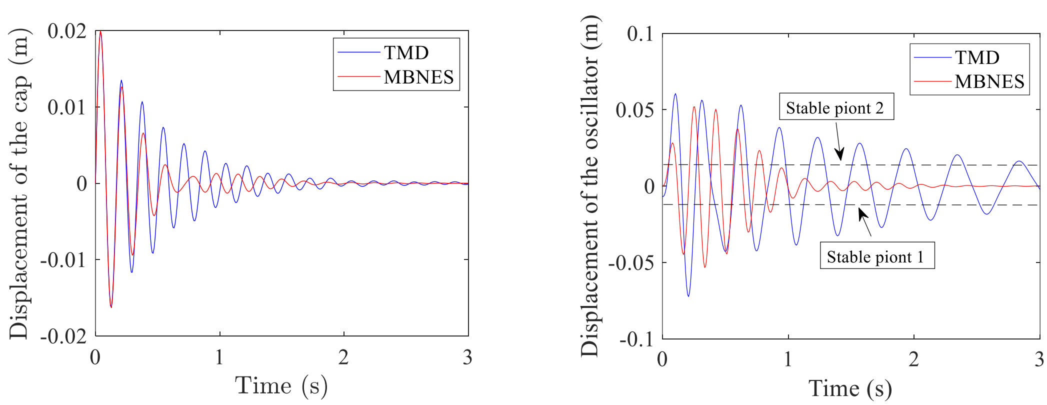

(a) (b)

Fig. 4 The displacement response of MBNES and TMD controlled structures under initial velocity excitation of 0.8 m/s: (a) caps; and (b) oscillators.

2.4 Identification of MBNES

In this study, the parameters for the magnet and spring in the MBNES that closely match the optimal ones available directly from the factory. For the experiment, the parameters 2*a*, 2*b* and 2*c* of magnets are 190 mm, 290 mm and 23 mm, respectively. The total stiffness of the two linear springs is 141.6 kN/m. The damping coefficient and stroke of VFD are 1.55 kN/(m/s) and ±80 mm. Due to the huge repulsion force of the magnets, d equal to 10 mm, it will be difficult to install. Therefore, it is opted for d=15 mm. Under the combination of these parameters, the value of I in Eq. (2) is 0.521.

In order to verify the accuracy of the restoring force curve of MBNES calculated via using Eq. (3), it is very necessary to use the restoring force surface method (RFM) to detect the nonlinear restoring force in the dynamical system [23,54-55]. To identify the parameters of the MBNES, the MBNES is attached to the shaking table. This is described by Eq.(7).

$$m_l \ddot{y} = f_e + f(y, \dot{y}) \tag{7}$$

Where y, $\dot{y}$ and $\ddot{y}$ are the relative (to the ground) displacement, velocity and acceleration of the oscillator. f_e is the externally applied force, $f_e = m_l \ddot{s}$. $\ddot{s}$ represents the acceleration of the shake table during the stepped sine motion. $f(y, \dot{y})$ is the restoring force of the MBNES, containing the nonlinear restoring and damping force. After getting the experimental data of y, $\dot{y}$, $\ddot{y}$ and f_e, the model for both the restoring force and damping force could be acquired. Fig. 5 is the experimental setup during the RFS test.

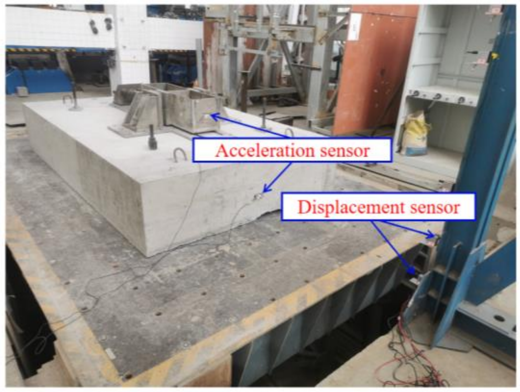

Fig. 5 The experimental setup using the restoring force surface method.

The velocity of the oscillator was obtained by taking the derivative of the displacement of the oscillator. A stepped sine motion with a frequency from 1 Hz to 5 Hz was applied to the shaking table. In Fig.6 (a), the red line represents the restoring force curve computed from experimental parameters of the MBNES via Eq.(3), and the blue points denote the $\dot{y} \approx 0$ data acquired during the stepped sine tests. Additionally, for Fig.6 (b), the red line is the desired damping restoring force curve and the blue points are the $y \approx 0$ data obtained from the RFS method. The agreement between the points obtained through the RFS method and the theoretically calculated curves validates the use of magnetic restoring force and damping force curve models in numerical analysis.

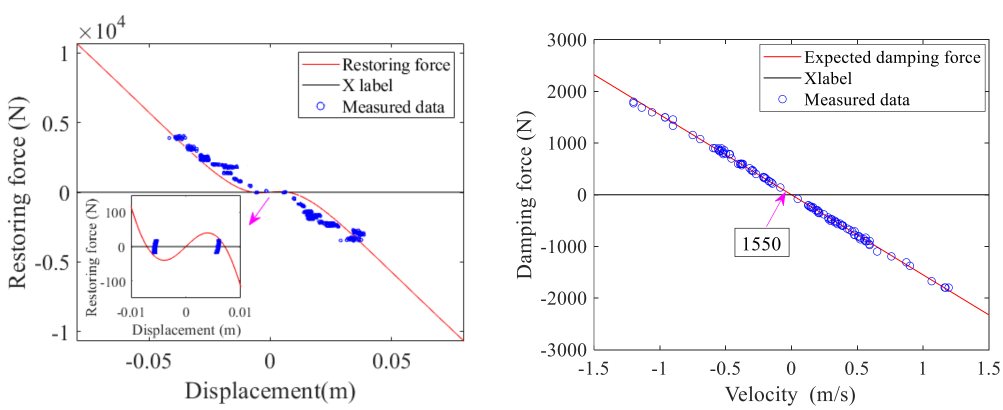

(a) (b)

Fig. 6 Restoring force curve and measured data: (a) the stiffness force; and (b) the damping force.

2.5 Seismic waves

Three seismic waves were selected as the loading conditions of this experiment: two natural ground motions (EL-Centro and TAFT seismic wave) and a synthetic seismic wave called RH2TG040, which was selected from the Pacific Earthquake Engineering Research Center. The waves have been time-compressed by 40% such that their dominant frequencies contain the natural frequency of the double-column piers. The time history and the frequency spectrum of three seismic waves are shown in Fig. 7(a) and Fig. 7(b). Where g is 9.8 m/s^2.

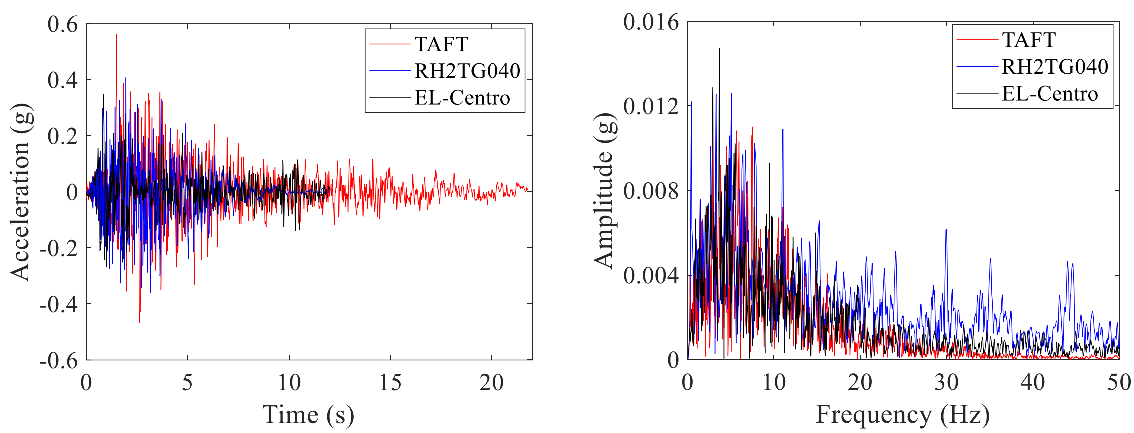

(a) (b)

Fig. 7 Three seismic ground motions: (a) Time-history; and (b) Spectrum analysis.

All seismic waves will be applied to the double-column piers with 5 peak ground accelerations (PGA) levels: 0.2g, 0.4g, 0.6g, 0.8g and 1.0g. White noise motion tests are applied to obtain the dynamic properties of the specimens before and after each seismic wave load action. For CIP-2, the oscillator is locked to obtain the dynamic characteristics of the whole structure. Table 3 exhibits the sequence of loading for the 3 different seismic waves with 5 different levels during the experiment.

Table 3 The input seismic waves for the experiment

No.	Seismic wave	PGA(g)	No.	Seismic wave	PGA(g)	No.	Seismic wave	PGA(g)
1	EL-Centro	0.2	6	RH2TG040	0.4	11	TAFT	0.8
2	TAFT	0.2	7	EL-Centro	0.6	12	RH2TG040	0.8
3	RH2TG040	0.2	8	TAFT	0.6	13	EL-Centro	1.0
4	EL-Centro	0.4	9	RH2TG040	0.6	14	TAFT	1.0
5	TAFT	0.4	10	EL-Centro	0.8	15	RH2TG040	1.0

3. Results and discussions

3.1 Damage process

The crack development and damage of CIP-1 (without MBNES) and CIP-2 (with MBNES) have been recorded in detail after each test condition referred in Table 3. The damage of the double-column piers after the experiment is illustrated in Fig. 8. Table 4 presents the detailed records of the damage process of the double-column piers during the whole experimental loading process. It shows that the MBNES is effective in slowing down the generation and development of cracks, attributed to the decreased displacement of the cap in CIP-2 thanks to the MBNES.

Table 4 The detailed double-column piers damage process during the experiment

No.	PGA(g)	Specimen	Experimental phenomena
1	0.2	CIP-1	A micro horizontal crack appeared at 70 mm from the top of the piers.
		CIP-2	No crack appeared.
2	0.4	CIP-1	An annular crack appeared at 170 mm from the top of the piers, and the initial crack extended to the pier's body
		CIP-2	Two horizontal cracks occurred at 30 mm and 110 mm from the top of the piers.
3	0.6	CIP-1	The initial crack developed into an annular crack, and the crack width became larger. Simultaneously, the oblique cracks appeared at 80 mm and 350 mm from the bottom of the piers.
		CIP-2	The initial crack at the pier top developed into an annular crack. In addition, two cracks at 140 mm and 210 mm from the top of the piers appeared. Meanwhile, a horizontal crack at 170 mm from the bottom of

			the piers appeared.
4	0.8	CIP-1	A shear crack appeared at 245 mm from the top of the piers, and two bending and shear inclined cracks also appeared at 130 mm and 260 mm from the bottom of the piers. Meanwhile, the initial crack at the bottom of the piers developed into an annular shear crack
		CIP-2	Three annular cracks formed at 70 mm, 140 mm and 320 mm from the top of piers, and two annular cracks generated at 10 mm and 170 mm from the bottom of piers.
5	1.0	CIP-1	The width of all the previous cracks increased, and some new cracks between the annular cracks appeared. At last, the concrete spalling occurred at the top of the pier as well as at the bottom.
		CIP-2	The bending and shear inclined cracks appeared at the top and bottom of the piers, and the width of the cracks which had occurred became larger. The concrete at the top and bottom of the piers had no spalling.

(a) (b)

Fig. 8 Damage patterns of the specimens: (a) CIP-1; and (b) CIP-2.

3.2 Dynamic characteristics

Because of the damage process, the natural frequency of the double-column piers decreases. After each test in the damage process, the natural frequency and damping ratio of each double-column piers were determined with a white-noise test of low PGA. The results are reported in Table 5. Before the damaging process, the natural frequency and damping ratio of CIP-1 and CIP-2 were almost the same. After the experiment, the natural frequencies of CIP-1 and CIP-2 are reduced by 52.1% and 42.9% and the damping coefficient of CIP-1 and CIP-2 increased by 109% and 91%, respectively. As the PGA increases, the natural frequency of each double-column piers decreases while the damping ratio increases, at varying rates for each. The natural frequency and damping ratio of CIP-2 is 18.72% higher and 7.73% lower than those of CIP-1. This means the MBNES can effectively reduce the impact on the stiffness decrease of the double-column piers and absorb the vibration energy in the double-column piers under the seismic wave load.

Table 5 The key spectral characteristics of the specimens after different seismic wave

Specimen	PGA(g)	0	0.2	0.4	0.6	0.8	1.0
CIP-1	Frequency (Hz)	5.91	5.85	4.56	3.37	3.16	2.83
CIP-2	Frequency (Hz)	5.89	5.87	4.93	4.13	3.61	3.36
CIP-1	Damping ratio (%)	5.19	5.29	5.99	7.43	8.87	10.86
CIP-2	Damping ratio (%)	5.23	5.26	5.61	6.62	8.19	10.02

3.3 Displacement and acceleration response

The peak displacement responses of the cap were also captured during the experiment. As revealed in Fig. 9 (a) to (c), the peak displacement increase with the increase of the PGA. For instance, when the PGA values of EL-Centro seismic wave were 0.2g, 0.4g, 0.6g, 0.8g, and 1.0g, the peak displacement of CIP-2 decreases by 78.2%, 47.5%, 36.0%, 24.9%, and 23.8% compared to CIP-1. This proves the vibration control performance of the MBNES over a wide range of natural frequencies.

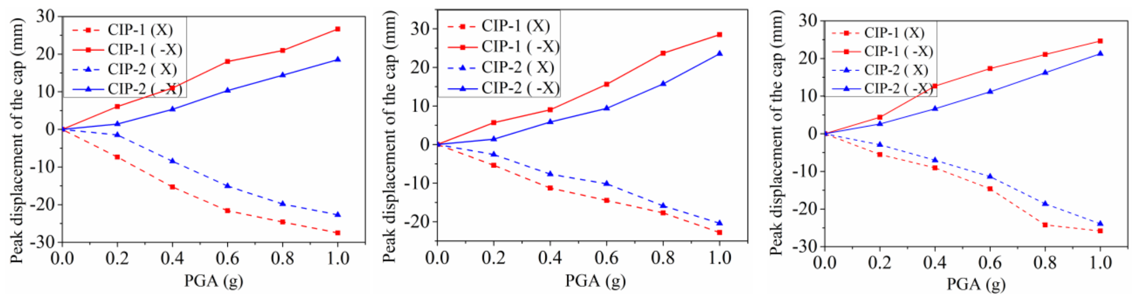

(a) (b) (c)

Fig. 9 Peak displacement response of the cap with the increase of PGA value of seismic wave: (a) EL-Centro; (b) TAFT; and (c) RH2TG040.

Fig. 10 compares the time evolution of the displacement of the cap for the PGA of 0.6g. For all seismic waves, the MBNES can effectively reduce the cap's displacement. For the PGA of 0.6g, EL-Centro, TAFT and RH2TG040 seismic waves, have $D_{RMS}/D_{RMS,0}$ of 0.6187, 0.6486, 0.6245, respectively. The MBNES can reduce the RMS displacement value of the cap by more than 35%. This reveals that MBNES can successfully absorb the energy transferred from the primary structure and dissipate it in time without reflecting it back to the primary structure. It is precisely because MBNES dissipates a lot of energy during the vibration that it can effectively reduce the internal force in the primary structure and reduce its damage.

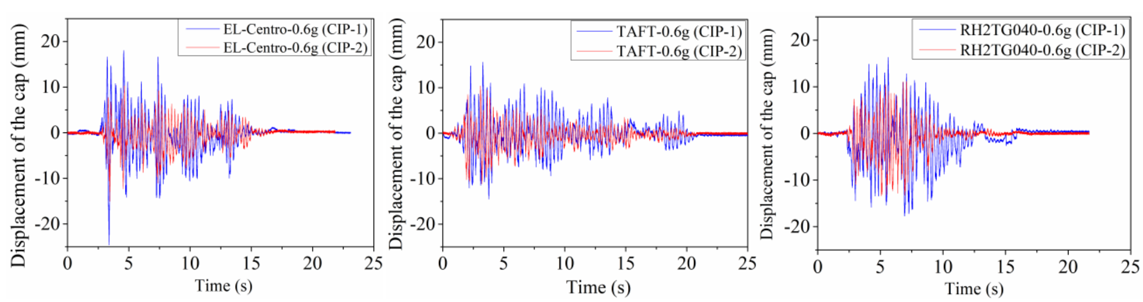

(a) (b) (c)

Fig. 10 The displacement of the cap under different seismic waves for the PGA is 0.6g: (a) EL-Centro; (b) TAFT; and (c) RH2TG040.

Fig. 11 depicts the displacement histories of the oscillator in the MBNES for the PGA of 0.6g. The oscillator has a large relative displacement during the whole seismic action process, more energy of the primary structure is transferred to the MBNES where the VFD subsequently dissipates it. During this process, the oscillator continuously transitioned between two stable points when the seismic energy input is high.

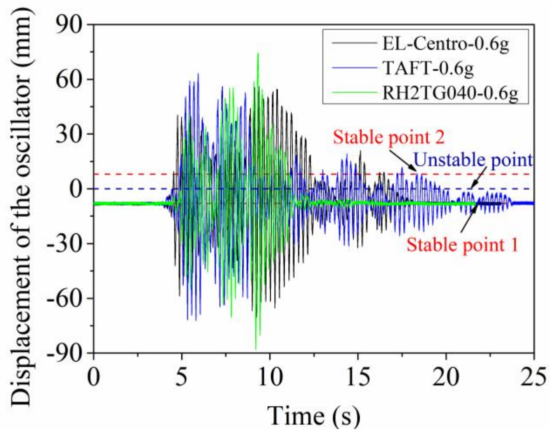

Fig. 11 The relative displacement of the oscillator under different seismic waves with the PGA value is 0.6g.

The peak acceleration responses of the cap are shown in Fig.12. When the PGA is less than 0.8g, the maximum acceleration responses of the CIP-2 cap are smaller than that of the CIP-1. Interestingly, when the PGA is 1.0g, the peak acceleration response of the CIP-2 cap is larger than that of CIP-1. This is because the natural frequency of CIP-1 is smaller than the dominant frequency of the seismic wave after experiencing seismic wave loads. However, the natural frequency of CIP-2 is still close to the dominant frequency of the seismic waves. This results in the seismic waves pumping more energy into the primary structure of CIP-2 and the response of the CIP-2 is more apparent.

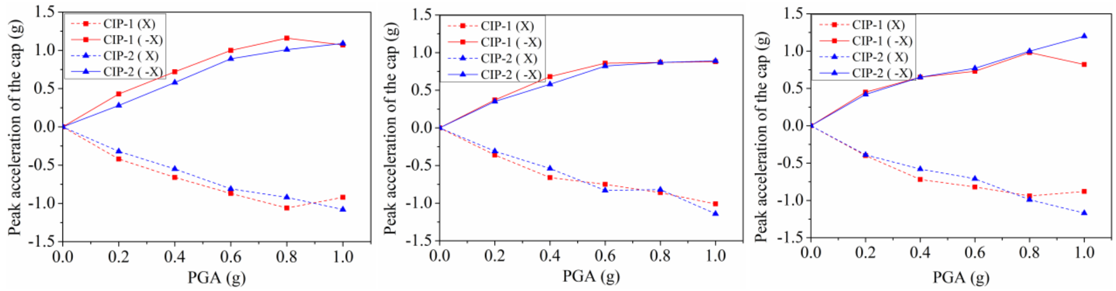

(a) (b) (c)

Fig. 12 The peak acceleration responses of the cap with the increase of PGA value of seismic wave: (a) EL-Centro; (b) TAFT; and (c) RH2TG040.

For PGA 0.6g the acceleration response of the cap are shown in Fig. 13 (a) to (c). The acceleration of the cap is almost consistent with that of the relative displacement. The RMS value of the cap's acceleration response of CIP-2 under the action of three seismic waves is reduced by 36.5%, 31.6% and 27.2%, respectively compared with CIP-1. It demonstrates that the MBNES can also effectively reduce the acceleration response of the primary structure.

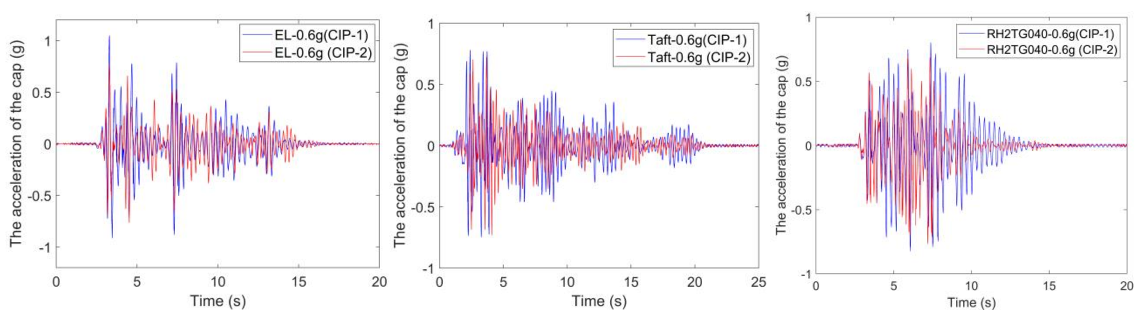

(a) (b) (c)

Fig. 13 The acceleration of the cap under different seismic waves with the PGA value is 0.6g: (a) EL-Centro; (b) TAFT; and (c) RH2TG040.

3.4 Curvature

The curvature was obtained and computed from vertical deformation measurements of the piers recorded by displacement sensors at 150 mm (S4 and S8) and 300mm (S3 and S7) below the cap and 150 mm (S1 and S5) and 300 mm (S2 and S6) above the footing. Here, the curvature of the piers under the action of EL-Centro wave is investigated. Eq. (8) computes the curvature φ [56]:

$$\varphi = \frac{\Delta_t - \Delta_c}{h_t b_t} \tag{8}$$

Where Δ_t and Δ_c represent the vertical displacement of the piers on the tension and compression sides, respectively. h_t is the distance between the measured curvature section and the footing or cap. b_t is the horizontal distance between the vertical displacement measurement points on both pier sides.

Fig.14 displays the curvature of the measured section of piers.The curvature of each section increases as the PGA value increases. Regardless of which PGA is applied, the curvature of the upper part is greater than that of the lower part of the piers, and the two curvatures have opposite directions, which is caused by the bending moment on the top of the pier being greater than that on the bottom of the pier. Meanwhile, the curvature of CIP-2 at each section of the column is smaller than that of CIP-1. For example, taking the section in piers of 150mm from the top surface of the footing into concerned, when the PGA is 0.2g, 0.4g, 0.6g, 0.8g and 1.0g, the curvatures of the X direction of CIP-1 are 0.027, 0.064, 0.14, 0.17 and 0.196 and of CIP-2 are 0.009, 0.022, 0.08, 0.128 and 0.18, respectively. Under the PGA of 0.6g, MBNES can effectively reduce the bending and damage of the piers. Although the effect of MBNES on reducing the curvature decreases when the PGA value of local seismic waves exceeds 0.6g, it is still not detuned and has good robustness. The other two seismic waves show a similar pattern.

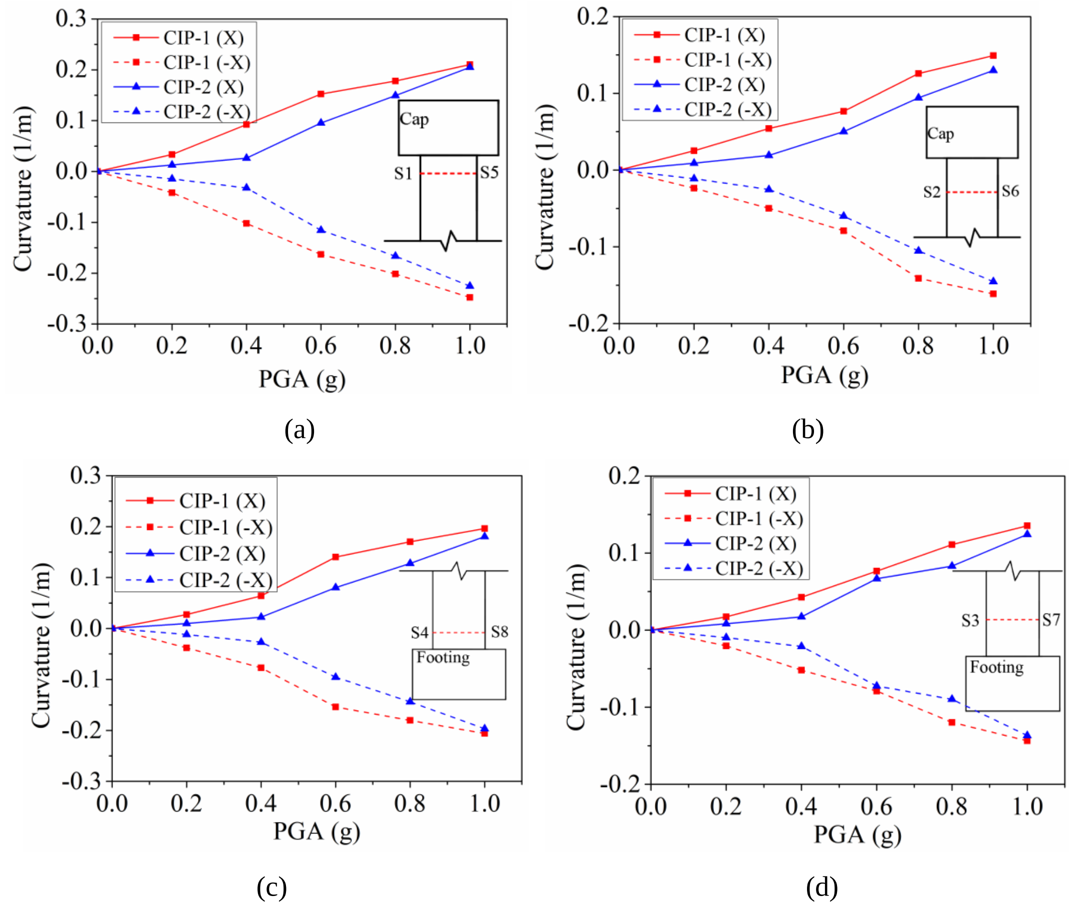

Fig. 14 Variation of curvatures under EL-Centro seismic wave: (a) at the height of 150 mm above the footing of the pier; (b) at the height of 300 mm above the footing of the pier; (c) at the height of 150 mm below the cap of the pier; and (d) at the height of 300 mm below the cap of the pier.

3.5 Shear deformation

Fig. 15 is the shear deformation of various parts of the pier under the action of El-Centro seismic wave. Section 1, section 2, section 3 and section 4 represent the 1200 mm to 1350 mm, 1050 mm to 1200 mm, 150 mm to 300 mm and 0 mm to 150 mm sections of the pier body, respectively. The shear deformation is the ratio of the difference between the top and bottom relative displacements of each section to the height of this section. The shear deformation at the upper part of the pier body is greater than that at the lower part of the pier body. This is mainly due to the large bending moment at the top of the pier body, which causes the upper part of the pier body to crack first. This reduces the stiffness of the section, resulting in a larger shear deformation than the bottom of the pier body. Moreover, because MBNES can effectively reduce the displacement of the cap under the same ground motion, the shear deformation of the CIP-2 pier body is smaller than that of CIP-1, especially under 0.6g PGA value. For example, take section 1 , when the PGA value of the EL-centro wave is 0.2g, 0.4g and 0.6g, the shear deformation of CIP-1 in the -X direction is -20.7×10^{-3}, - 33×10^{-3} and -47.2×10^{-3}, while the shear deformation of CIP-2 is -12.73×10^{-3}, -23.2×10^{-3} and -36.8×10^{-3}, which were respectively reduced by 38.5%. 29.7% and 22.1%.

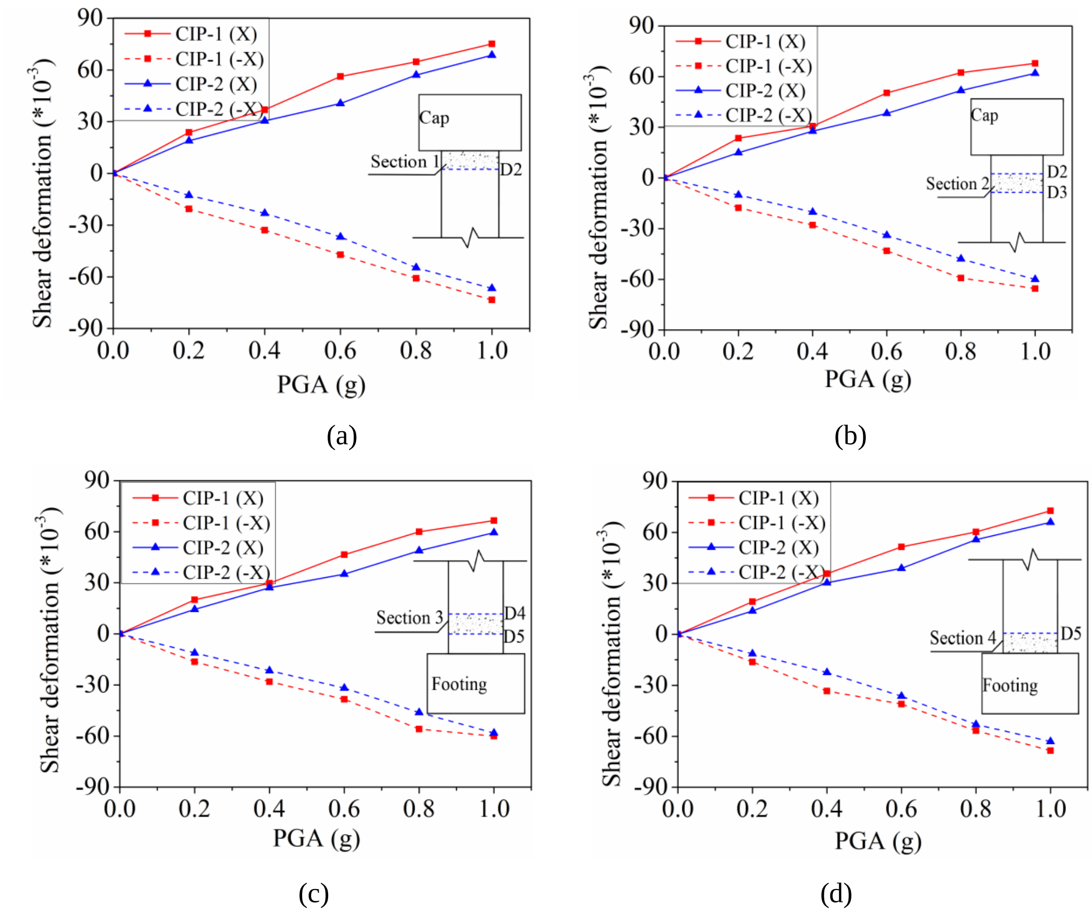

Fig. 15 The shear deformation of each section of the pier under El-Centro seismic wave: (a) Section 1;

(b) Section 2; (c) Section 3; and (d) Section 4.

4. Numerical performance

4.1 System description with Bouc-Wen model

Considering that the concrete double-column piers are damaged during the vibration process, their stiffness will be changed. The Bouc-Wen model, which can describe the stiffness change of the piers during the seismic wave excitation [57]. Therefore, Eq. (1) is transformed to Eq. (9).

$$\begin{cases} m_p\ddot{x}_p + c_p\dot{x}_p + F_p(x_p, z) - c_l\dot{u} - F = -m_p\ddot{x}_g \\ m_l\ddot{u} + c_l\dot{u} + F = -m_l(\ddot{x}_g + \ddot{x}_p) \end{cases} \tag{9}$$

Where z is the hysteretic deformation of the primary structure. $F_p(x_p, z)$ is the restoring force of the primary structure and calculated by Eq. (10) .

$$\begin{cases} F_p(x_p, z) = \alpha k_p x_p + (1-\alpha)k_p z \\ \dot{z} = \delta\dot{x}_p - \beta|\dot{x}_p||z|^{\mu-1}z - \eta\dot{x}_p|z|^{\mu} \end{cases} \tag{10}$$

Where α is the stiffness ratio after yielding to the initial stiffness and is set as 1/21. β, η and μ are the parameters controlling the hysteresis loop's shape, size and smoothness. For reinforced concrete structures, the value of μ is 2, β=-3η, and η is set as -1/2, β is 3/2 [58]. δ usually set as 1 [59-60]. Other parameters of the primary structure are the same as the initial values of the test. Considering that the specimen is subjected to continuous seismic wave excitation, when the PGA of the seismic wave exceeds 0.4g, the damage of the primary structure leads to the change of the initial stiffness at each test. This will lead to changes in the parameters in the Bouc-Wen model. Therefore, this study only conducts numerical analysis on the response under EL-Centro seismic wave excitation for PGA is

0.6g. Fig.16 compares the numerical analysis and experiment displacement time-history curves of CIP-1 and CIP-2 under EL-Centro seismic wave excitation. The ratio of RMS values from the experiment to the numerical analysis of CIP-1 and CIP-2 are 1.0744 and 1.0983, that the Bouc-Wen model can effectively predict the displacement response of double-column piers under seismic wave loads.

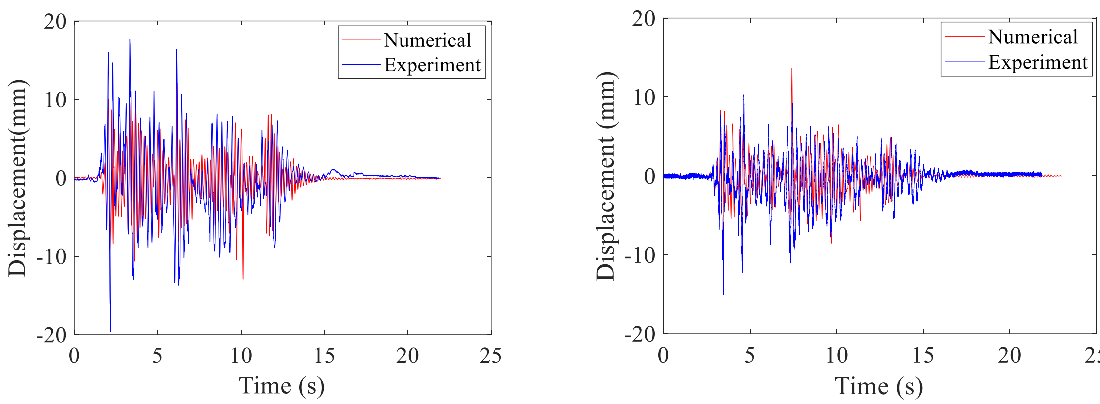

(a) (b)

Fig. 16 Comparison of numerical analysis and experimental results: (a) CIP-1; and (b) CIP-2.

Wavelet transform is applied to obtain the energy density distribution of each specimen in the time domain and frequency domain during the vibration process. Morlet wavelet is used as the mother wavelet on the acceleration of the cap of CIP-1, the cap of CIP-2 and MBNES oscillator under of EL-Centro loading with 0.6g PGA value of 0.6g. Fig. 17 (a) to (c) show the time-dependent frequency behavior of the visualized responses. The energy of specimen CIP-1 is concentrated between 4.56 Hz and 3.37 Hz, and the energy of specimen CIP-2 is mainly concentrated between 4.93 Hz and 4.13 Hz, which is consistent with the change of the natural frequency shown in table 4. The energy distribution density of specimen CIP-1 during loading time is higher than that of specimen CIP-2, indicating that its energy dissipation rate is slower than that of specimen

CIP-2. In addition, the frequency of energy distribution in MBNES is mainly concentrated between 4.93 Hz and 4.13 Hz, which means that MBNES can generate internal resonance with the primary structure, absorb the vibration energy from the primary structure and dissipate it. This also indicates that the MBNES has a broadband performance.

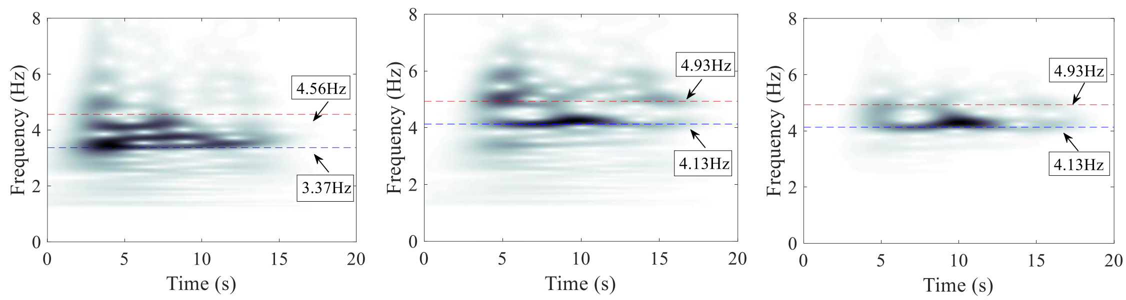

(a) (b) (c)

Fig. 17 Wavelet spectra of acceleration under EL-Centro seismic waves with the PGA value is 0.6g: (a) CIP-1; (b) CIP-2; and (c) MBNES.

4.2 Robustness observation

Considering the complexity and variability of the frequency components of each seismic wave and the changes to the dynamic characteristics of the primary structure under increased loading, the robustness of the oscillator is crucial here. Here, the MBNES and the TMD will be compared, numerically. Fig. 18 shows the changes of $E_p/E_{p,0}$ with the stiffness changes of the primary structure under the action of three seismic waves when the PGA is 0.4g. As the stiffness of primary structure decreases, the MBNES still retain its effective response suppression for the primary structure, whereas the TMD experiences a loss in suppression efficiency to some degree. Specifically, When the stiffness of the primary structure is 100% to 40% of the initial stiffness, $E_p/E_{p,0}$ with

MBNES (dotted lines) is lower than that of TMD (full lines). That means the nonlinear characteristic in the MBNES enhances the robust performance in vibration absorption and can absorb vibration at a wider frequency range than the TMD.

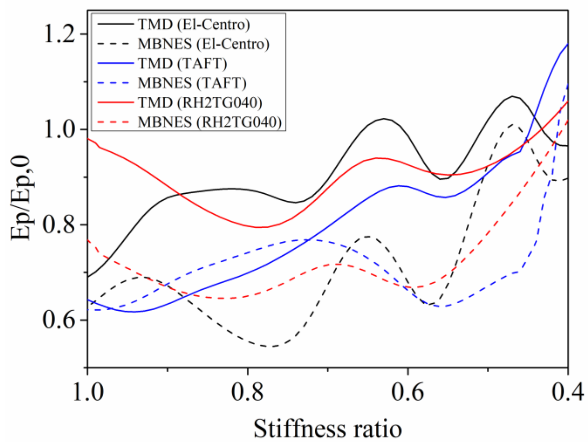

Fig. 18 Response trends of $E_p/E_{p,0}$ with stiffness variations of the primary structure under different seismic wave loads.

The energy input of the system is also an important factor that affects the robustness of the oscillator. Fig. 19 (a) to (c) show the influence of the PGA of different seismic waves on the energy response of the primary structure. With the PGA value increases from 0.2g to 1.0g, the MBNES can consume more energy from the primary structure compared to the TMD, and the gap in energy consumption is becoming more and more obvious. This means that using the proposed MBNES has better robustness to the response to different seismic waves than TMD control.

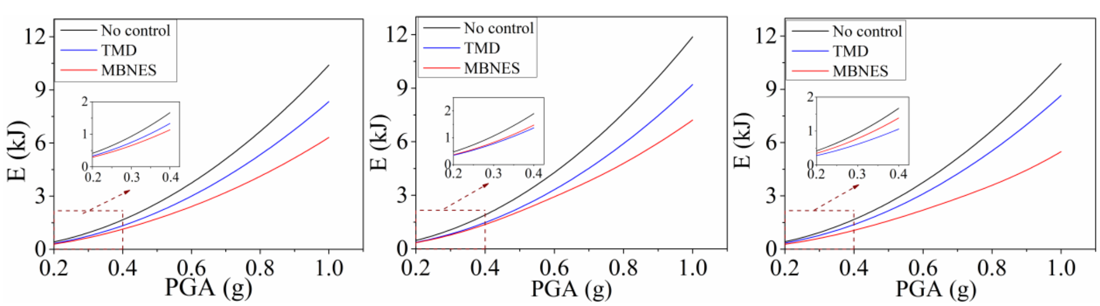

(a) (b) (c)

Fig. 19 Effect of PGA values on the energy response under different seismic waves load: (a) EL-Centro; (b) TAFT; and (c) RH2TG040.

5. Conclusion

This study presents the experimental tests and numerical simulations of the double-column piers damped by a magnetic bi-stable nonlinear energy sink (MBNES) consisting of springs, magnets, and a viscous fluid damper (VFD). The structural construction of the double-column piers, the seismic waves used for excitation, and the sensors arrangement of the specimen were elaborated. Through shaking table tests and numerical analysis, the following conclusions are obtained.

1. The dimensions of the magnets, the springs and damping of the MBNES are determined from global optimization method for the proposed objective function. The optimization proposed, along with readily available parts, enables the design's adaptability for use in diverse civil structures. The experimental identification with the restoring force surface method MBNES are in good agreement with the expected theoretical restoring force calculation.

2. From the shaking table test of CIP-2 with MBNES and CIP-1 (without MBNES), it can be found that MBNES can effectively reduce the damage in double-column piers. Furthermore, due to the effective vibration absorption of MBNES, compared with CIP-1, CIP-2 has been effectively controlled in terms of stiffness reduction, displacement, acceleration, curvature and shear deformation of the double-column piers.

3. Numerical analysis simulates the time-history response of the two piers under

seismic wave excitation, with the primary structure adopting the Bouc-Wen model, which can describe the hysteretic performance of concrete piers. In addition, wavelet transform is used to analyze the energy distribution of the primary structure and MBNES during the seismic wave action. Finally, the robustness of the MBNES and the TMD is analyzed, and it is verified that the MBNES has wide-frequency band damping characteristics and acceptable robustness.

Acknowledgment

The authors gratefully acknowledge the National Natural Science Foundation of China (Grant No.51878151) and China Scholarship Council (No.202206090067). At the same time, we would like to thank all the reviewers who provided constructive comments on this article for their hard work.

References:

[1] Pinkaew T, Lukkunaprasit P, Chatupote P. Seismic effectiveness of tuned mass dampers for damage reduction of structures. Eng Struct 2003 Jan; 25(1):39-46.

[2] Rahimi F, Aghayari R, Samali B. Application of tuned mass dampers for structural vibration control: A state-of-the-art review. Civil Engineering Journal-Tehran 2020 Aug; 6(8):1622-1651.

[3] Ding H, Chen LQ. Design, analysis, and applications of nonlinear energy sinks. Nonlinear Dynam 2020 Jun 19; 100(04):3061-3107.

[4] Vakakis AF, Gendelman OV, Bergman LA, Mojahed A, Gzal, M. Nonlinear targeted energy transfer: state of the art and new perspectives. Nonlinear Dynam 2022 Feb 10; 108(02):711-741.

[5] Gourdon E, Lamarque CH. Energy pumping with various nonlinear structures: numerical evidence. Nonlinear Dynam 2005 May 1; 40(03): 281-307.

[6] Gourdon E, Lamarque CH. Energy pumping for a larger span of energy. J Sound Vib 2005 Jul 22; 285(03):711-720.

[7] Gourdon E, Alexander NA, Taylor CA, Lamarque CH, Pernot S. Nonlinear energy pumping under transient forcing with strongly nonlinear coupling: theoretical and experimental results. J Sound Vib 2007 March 6; 300(3-5):522-551.

[8] Gourdon E, Lamarque CH, Pernot S. Contribution to the efficiency of irreversible passive energy pumping with a strong nonlinear attachment. Nonlinear Dynam 2007 Dec 1; 50(04): 793-808.

[9] Nucera F, IaconoFL , McFarland DM, Bergman LA, Vakakis AF. Application of broadband nonlinear targeted energy transfers for seismic mitigation of a shear frame: Experimental results. J Sound Vib 2008 Jun 3; 313(1-2):57-76.

[10] Quinn DD, Hubbard S, Wierschem N, Al-Shudeifat MA, Ott RJ, Luo J, Spencer BF, McFarland DM, Vakakis AF, Bergman LA. Equivalent modal damping, stiffening and energy exchanges in multi-degree-offreedom systems with strongly nonlinear attachments. P I Mech Eng K-J Mul 2012 Jan 1; 226(K2):122-146.

[11] Saeed AS, Nasar RA, AL-Shudeifat MA. A review on nonlinear energy sinks: designs, analysis

and applications of impact and rotary types. Nonlinear Dynam 2023 Jan; 111(01):1-37.

[12] Al-Shudeifat MA, Wierschem NE, Bergman LA, Vakakis AF. Numerical and experimental investigations of a rotating nonlinear energy sink. Meccanica 2017 Mar 29; 52(4-5):763-779.

[13] Saeed AS, AL-Shudeifat MA,Vakakis AF, Cantwell WJ. Rotary-impact nonlinear energy sink for shock mitigation: analytical and numerical investigations. Archive of Applied Mechanics 2020 Mar 5;90(03)495-521.

[14] Saeed AS, AL-Shudeifat MA, Vakakis AF. Rotary-oscillatory nonlinear energy sink of robust performance. Int J Nonlin Mech 2019 Dec;117:103249.

[15] Wierschem NE, Quinn DD, Hubbard SA, Al-Shudeifat MA, McFarland DM, Luo J, Fahnestock LA, Spencer BF, Vakakis AF, Bergman LA. Passsive damping enhancement of a two-degree-of-freedom system through a strongly nonlinear two-degree-of-freedom attachment. J Sound Vib 2012 Dec 3; 331(25), 5393-5407.

[16] Wierschem NE, Luo J, Al-Shudeifat M, Hubbard S, Ott R, Fahnestock LA, Quinn DD, McFarland DM, Spencer BF, Vakakis A, Bergman LA. Experimental testing and numerical simulation of a six-story structure incorporating two-degree-of-freedom nonlinear energy sink. J Strct Eng 2014 Jun 1;140(6):4014027.

[17] Wierschem NE, Hubbard SA, Luo J, Fahnestock LA, Spencer BF, McFarland DM, Quinn DD, Vakakis AF, Bergman, LA. Response attenuation in a large-scale structure subjected to blast excitation utilizing a system of essentially nonlinear oscillators. J Sound Vib 2017 Feb 17; 389:52-72.

[18] Wierschem NE, Luo J, Wilcoski J, Hubbard SA, Fahnestock LA, Spencer BF, McFarland DM, Quinn DD, Vakakis AF, Bergman LA. Simulating offset blast loads experimentally using shake-table-generated ground motions: Method development and validation. Struct Control Hlth 2020 Feb; 27(2):e2480.

[19] Wang JJ, Wierschem NE, Spencer BF, Lu XL. Track nonlinear energy sink for rapid response reduction in building structures. J Een Mech 2015 Jan; 141(01):1-10.

[20] Wang JJ, Wierschem NE, Spencer BF, Lu XL. Experimental study of track nonlinear energy

sinks for dynamic response reduction. Eng Struct 2015 Jul 1; 94:9-15.

[21] Wang JJ, Wierschem NE, Spencer BF, Lu XL. Numerical and experimental study of the performance of a singlesided vibro-impact track nonlinear energy sink. Earthq Eng Struct D 2016 Apr 10; 45(04):635-652.

[22] Wang JJ, Wierschem NE, Wang B, Spencer BF. Multi-objective design and performance investigation of a high-rise building with track nonlinear energy sinks. Struct Design Tall Spec Build 2020 Feb 10; 29(02):e1692.

[23] Dekemele K, Van Torre P, Loccufier M. Design,construction and experimental performance of a nonlinear energy sink in mitigating multi-modal vibrations. J Sound Vib 2020 May 12; 473:115243.

[24] Dekemele K, Keyser RD, Loccufier M. Performance measures for targeted energy transfer and resonance capture cascading in nonlinear energy sinks. Nonlinear Dynam 2018 Mar 12; 93:259-284.

[25] Gourdon E, Alexander NA, Taylor CA, Lamarque CH, Pernot S. Nonlinear energy pumping under transient forcing with strongly nonlinear coupling: theoretical and experimental results. J Sound Vib 2007 Mar 6; 300(3-5):522-551.

[26] Georgiadis F, Vakakis AF, Mcfarland DM, Bergman L. Shock isolation through passive energy pumping caused by nonsmooth nonlinearities. Int J Bifurc Chaos 2005 Jun 1; 15(06): 1989-2001.

[27] Nucera F, Vakakis AF, McFarland DM, Bergman LA, Kerschen G. Targeted energy transfers in vibroimpact oscillators for seismic mitigation. Nonlinear Dyn 2007 Nov 1; 50(03): 651-677.

[28] Panagopoulos PN, Vakakis AF, Tsakirtzis S. Transient resonant interactions of finite linear chains with essentially nonlinear end attachments leading to passive energy pumping. Int J Solids Struct 2004 Nov 1; 41(22-23):6505-6528.

[29] Tsakirtzis S, Kerschen G, Panagopoulos PN, Vakakis AF. Multi-frequency nonlinear energy transfer from linear oscillators to mdof essentially nonlinear attachments. J Sound Vib 2005 Jul 6; 285(1-2):483-490.

[30] Lv XL, Liu ZP, Lu Z. Optimization design and experimental verification of track nonlinear energy sink for vibration control under seismic excitation. Struct Control Heal Monit 2017 May 5;

24(12): e2033.
[31] Andersen D, Starosvetsky Y, Vakakis A, Bergman L. Dynamic instabilities in coupled oscillators induced by geometrically nonlinear damping. Nonlinear Dyn 2012 Apr 6; 67(01): 807-827.
[32] Kong XR, Li HQ, Wu C. Dynamics of 1-dof and 2-dof energy sink with geometrically nonlinear damping: application to vibration suppression. Nonlinear Dyn 2018 Jun 23; 91(01)733-754.
[33] Liu Y, Mojahed A, Bergman L, Vakakis AF. A new way to introduce geometrically nonlinear stiffness and damping with an application to vibration suppression. Nonlinear Dyn 2019 Mar 23; 96(02): 1819-1845.
[34] Al-Shudeifat MA. Highly efficient nonlinear energy sink. Nonlinear Dyn 2014 Jan 30; 76(04): 1905-1920.
[35] Manevitch LI, Sigalov G, Romeo F, Bergman LA, Vakakis A. Dynamics of a linear oscillator coupled to a bistable light attachment: analytical study. J Appl Mech 2013 Apr; 81(04):041011.
[36] Romeo F, Sigalov G, Bergman LA, Vakakis AF. Dynamics of a linear oscillator coupled to a bistable light attachment: numerical study. J. Comput. Nonlinear Dyn 2014 Sep 12; 10(01):011007.
[37] Dekemele K, Habib G, Loccufier M. The periodically extended stiffness nonlinear energy sink. Mech Syst Signal Pr 2022 Apr 15; 169:108706.
[38] Lo Feudo S, Touze C, Boisson J, Cumunel G. Nonlinear magnetic oscillator for passive control of a multi-storey structure. J Sound Vib 2019 Jan 6; 438:33-53.
[39] Luo J, Wierschem NE, Fahnestock LA, Spencer BF, Quinn DD, McFarland DM, Vakakis AF, Bergman LA. Design, simulation, and large-scale testing of an innovative vibration mitigation device employing essentially nonlinear elastomeric springs. Earthq Eng Struct Dyn 2014 Oct 10; 43(12):1829-1851.
[40] Al-Shudeifat MA. Asymmetric magnet-based nonlinear energy sink. J Comput Nonlinear Dynam 2015 Jan 1; 10(01):014502.
[41] Chen YY, Qian ZC, Zhao W, Chang CM. A magnetic Bi-stable nonlinear energy sink for structural seismic control. J Sound Vib 2020 May 12; 473:115233.

[42] Chen YY, Su WT, Tesfamariam S, Qian ZC, Zhao W, Shen CY, Zhou FL. Experimental testing and system identification of the sliding bistable nonlinear energy sink implemented to a four-story structure model subjected to earthquake excitation. Journal of Building Engineering 2022 Dec 1; 61:105226.

[43] Chen YY, Su WT, Tesfamariam S, Qian ZC, Zhao W, Yang ZY, Zhou FL. Experimental study of magnetic bistable nonlinear energy sink for structural seismic control. Soil Dyn Earthq Eng 2023 Jan; 164:107572.

[44] Geng XF, Ding H, Jing XJ, Mao XY, Wei KX, Chen LQ. Dynamic design of a magnetic-enhanced nonlinear energy sink. Mech Syst Signal PR 2023 Feb 15; 185:109813.

[45] Zeng YC, Ding H. A tristable nonlinear energy sink. Int J Mech SCI 2023 Jan 15; 238:107839.

[46] Yao H, Zheng D, Wen B. Magnetic nonlinear energy sink for vibration attenuation of unbalanced rotor system. Shock Vib 2017 Dec 14; 2017:4132607.

[47] Yang HX, Yang BL, Wang HB, Zhang MH, Ni SY. Research on dynamic characteristics of joint of RC frame structure with NES. Sustainability 2022 Sep; 14(18):11229.

[48] Ministry of housing and urban rural development of the people's Republic of China. Standard for test method of concrete structures. GB/T 50152-2012. Beijing, China.

[49] China National Standardization Administration Committee. Metallic materials-tensile testing at ambient temperature. GB/T228.1-2010. Beijing, China.

[50] Ministry of Transport of the People's Republic of China. Specifications for seismic design of highway bridge. JTG/T 2231-01-2020. Beijing, China.

[51] Chen YY, Qian ZC, Chen K, Tan P, Tesfamariam S. Seismic performance of a nonlinear energy sink with negative stiffness and sliding friction. Struct Control Health. 2019 Aug 14; 26(11):e2437.

[52] Luo J, Wierschem NE, Hubbard SA, Fahnestock LA, Quinn DD, McFarland DM, Spencer BF, Vakakis AF, Bergman LA. Large-scale experimental evaluation and numerical simulation of a system of nonlinear energy sinks for seismic mitigation. Eng Struct 2014 Oct 15; 77:34-48.

[53] Rana R, Soong TT, Parametric study and simplified design of tuned mass dampers. Eng Struct

1998 Mar; 20(3):193-204.

[54] Kerschen G, Worden K, Vakakis AF, Golinval JC. Past, present and future of nonlinear system identification in structural dynamics. Mech Syst Signal Pr 2005 Oct 7; 20(3):505-592.

[55] Noël J, Kerschen G. Nonlinear system identification in structural dynamics: 10 more years of progress. Mech Syst Signal Pr 2017 Jan 15; 83:2-35.

[56] Varma AH, Ricles JM, Sause R, Lu LW. Seismic behavior and design of high-strength square concrete-filled steel tube beam columns. J Struct Eng 2004 Feb 1; 130(2):169-179.

[57] Wen YK. Method for random vibration of hysteretic systems. J Eng Mech 1976 Jan 1; 102(2): 249-263.

[58] Li GQ, Cao H. Structural dynamic reliability theory and Application. 1st edit. Beijing: Seismological Press; 1993.

[59] Tsiatas GC, Charalampakis AE. A new hysteretic nonlinear energy sink (HNES). Commun. Nonlinear Sci Numer Simul 2018 Mar 2; 60:1-11.

[60] Foliente GC, Singh MP, Noori MN. Equivalent linearization of generally pinching hysteretic, degrading systems. Earthquake Eng Struct Dyn 1996 Jun 1; 25(6):611-629.